






Article

Effects in Band Gap for Photocatalysis in TiO₂ Support by Adding Gold and Ruthenium

Omar Ricardo Fonseca-Cervantes ¹, Alejandro Pérez-Larios ²,
Víctor Hugo Romero Arellano ¹, Belkis Sulbaran-Rangel ¹ and
Carlos Alberto Guzmán González ^{3,*}

¹ Department of Water and Energy, University of Guadalajara Campus Tonalá, Tonalá 45425, Mexico; omar.fonseca9003@alumnos.udg.mx (O.R.F.-C.); vicromare@gmail.com (V.H.R.A.); belkis.sulbaran@academicos.udg.mx (B.S.-R.)

² Materials, Water and Energy Laboratory, Department of Engineering, University of Guadalajara Campus Altos, Tepatitlán de Morelos 47635, Mexico; alarios@cualtos.udg.mx

³ Department of Applied Basic Sciences, University of Guadalajara Campus Tonalá, Tonalá 45425, Mexico

* Correspondence: carlosalberto.guzman@cutonala.udg.mx; Tel.: +52-3320002300 (ext. 64029)

Received: 30 July 2020; Accepted: 21 August 2020; Published: 24 August 2020



Abstract: One of the key features of a nano catalyst for photocatalysis is the band gap, because, through its analysis, the potential of the catalyst can be determined. In this investigation, the impact on the band gap of different catalysts made by the sol–gel method, compared with TiO₂ P25 Sigma-Aldrich, showing the effect of using gold or ruthenium as a metal supported on TiO₂, with two different dosage percentages of 1 and 3 percent, was analysed. Additionally, two oxidation states of the catalyst, the reduced form and the oxidized form of the metal, were used to see the effect on the band gap. The experiments show that the gold addition has a higher beneficial effect on the band gap for the UV region (ultra violet region), and the ruthenium addition has a higher beneficial effect for the UV/visible region. The preferred oxidation state for the band gap was the oxidized state. The characterisation of the catalyst provided an insight into the relation between the band gap and the catalyst itself.

Keywords: photocatalysis; sol–gel method; supported on TiO₂; oxidized and reduced oxidation states

1. Introduction

Photocatalysis is a process of great interest because, in recent years, it has been shown to have wide applications in environmental decontamination processes because it can degrade a wide variety of organic compounds like sugars [1]. The use of solar energy to degrade pollutants through photocatalysis represents an economic and sustainable alternative when the advanced oxidation process (AOP) is considered for decontamination [2]. Heterogeneous photocatalytic solar oxidation consists of using near-solar UV radiation (wavelength less than 380 nm; energy levels larger than 3.2 eV) to photo-excite a semiconductor catalyst in the presence of oxygen. Under these circumstances, the oxidation of the pollutants takes place.

The TiO₂ semiconductor is normally used as a catalyst by absorbing light of different wavelengths owing to their electronic structure, characterized by an empty conduction band and with a filled valence band [3]. The photocatalytic process takes place from the irradiation of light with sufficient energy to equal or exceed the band-gap of the semiconductor, causing the excitation of an electron from the valence band (VB) to the conduction band (CB) [3]. In this way, electron–hole pairs (e[−]/h⁺) are created that can migrate to the surface of the catalyst, being trapped in superficial sites and reacting with the adsorbed species [4]. The voids (empty states) that form in the valence band of the solid react with electron-donating species, such as water molecules or hydroxyl ions attached to the surface of

the catalyst, generating hydroxyl radicals ($\bullet\text{OH}$), which are mainly responsible for the degradation of organic matter. In turn, the electrons that reach the conduction band can react with a receptor species such as O_2 giving rise to O_2^- radicals, which further participate in the oxidation of organic matter. However, in competition with the charge transfer processes, recombination processes take place in which the electron-hole pair recombines before reacting with the species adsorbed on the catalytic surface. The final efficiency of the photocatalytic reaction depends on many factors that determine the degree of total oxidation of the organic matter. The probability of the electron-gap pair recombination on the surface of the semiconductor material results in a critical process because there is no physical separation between the sites of anodic (gap oxidation) and cathodic (electron reduction) reactions [5].

There is a significant amount of literature on the preparation of supported metal catalysts [6–8]. Many combinations of metal and support are possible, and the catalysts can be prepared by different techniques, for example, sol-gel, impregnation, co-precipitation, deposition-precipitation, and controlled surface reaction [9]. On this basis, the catalytic activity can be sensitive to the method of preparation and the oxide-reduction heat treatments. The sol-gel method consists of the formation of solid networks, composed of inorganic elements, which are obtained from the hydrolysis of an alkoxide, alcohol, and water, called sol. In the sol, micelles are suspended in the liquid form, and increase in size (1–100 nm) as a function of time in a constant agitation system, until the gel is formed. The gel is a polymeric system that, when dried, forms a powder that is mainly used to obtain colloidal oxides, ceramic materials that serve as heterogeneous supports, or catalysts [10]. In the present study Au/TiO₂ (gold supported on titanium oxide) and Ru/TiO₂ (ruthenium supported on titanium oxide) catalysts (1 and 3% by weight) were prepared in their oxidized and reduced forms by the sol-gel method. It was decided to use ruthenium (Ru), because its effectiveness as a catalyst has already been reported under different percentages from 0.2% to 5% and in different contaminants such as hydrogenation and the reduction of carbon dioxide [11], to hydrogenate levulinic acid [12] and degradation of 2-chlorophenol under visible light [6]. In the case of gold (Au), its effectiveness as a catalyst in the degradation of pollutants has also been demonstrated [7,13] and, when compared with other precious metals such as palladium (Pd) and platinum (Pt), its cost is lower and it has presented greater activity, stability, and selectivity as a catalyst [14]. The novelty of this research is that it compares the TiO₂ supported catalyst with the high anatase content. The metals are added (gold or ruthenium) at different percentages (1 wt.% and 3 wt.%) and different oxidation states of the metal (reduced and oxidized) to determine the impact of the metal size in the photocatalytic activity through energy band gap measurements.

2. Materials and Methods

2.1. Materials

Titanium (IV) butoxide ($\text{Ti}(\text{OCH}_2\text{CH}_2\text{CH}_2\text{CH}_3)_4$) reagent grade, 97%, used as a support for the catalyst in the sol-gel method, was purchased from Sigma-Aldrich. The TiO₂ P25 was also purchased from Sigma-Aldrich, reagent grade 99.5%. The ruthenium (Ru) precursor, ruthenium (III) chloride hydrate with ruthenium content, 40–49% ($\text{RuCl}_3 \times \text{H}_2\text{O}$), and the gold (Au) precursor, gold (III) chloride trihydrate $\geq 99.9\%$ trace metals ($\text{HAuCl}_4 \cdot 3\text{H}_2\text{O}$), were purchased from Sigma-Aldrich. The acids used to reach pH in the preparation methods, nitric acid (HNO_3) reagent at 65% and hydrochloric acid (HCl) reagent at 37%, were purchased from Sigma-Aldrich. The ethyl alcohol (99.8%) was purchased from J.T. Baker. The hydrogen (>99.9%) gas used for the reduction process for the catalyst was purchased from Praxair (Linde).

2.2. Sol-Gel Method for Preparing the TiO₂ Support

The sol-gel synthesis procedure of the TiO₂ support was according to the method reported by Rodríguez-González [15]. First, the proper amount of ethanol and water in the molar ratio 2:1 was prepared at pH \approx 3 (nitric acid). The alkoxide solution was made with the titanium (IV)

butoxide and water in a molar ratio of 1:8. The ethanol/water mix was stirred at 75 °C. The use of a condenser is required with a refrigerant recirculation at 5 °C. After the ethanol/water mix reached 75 °C, the alkoxide/water mix was added drop by drop to the ethanol/water mix. After all the alkoxide solution was added, the solution underwent continuous stirring at reflux for 24 h at 75 °C. After 24 h, the solution was transferred to a rotary evaporator in a water bath at 60 °C for 1 h, and the pressure conditions were changed to produce a vacuum. The initial pressure was 810 mbar and the final pressure was 100 mbar for 150 min. The solution was evaporated, and the final material was taken out to dry in an oven for 24 h at 120 °C. The material was then calcined for 4 h at 500 °C. After that time, the material was introduced to a desiccator for 24 h to reach ambient temperature. Finally, the material was ground ready to be used as a support.

2.3. Synthesis of Gold and Ruthenium Nanoparticles

The support made by the sol–gel method was used to add metals. The Au- and Ru-loaded TiO₂ nanoparticles were prepared by an impregnation method [10]. The proper material balance to get 1 wt.% (weight percentage) and 3 wt.% was made for each metal.

The process was conducted in acid conditions, pH ≈ 2 (HCl). The dissolution of the support was made in water and the pH was adjusted with the acid. The solution of the support in water was stirred for 2 h and the solution of the metal was made by dissolving the proper amount (in two different proportions) of the metal salt in water and stirring for 2 h. The metal salt solution was added to the support solution and the resulting solution was stirred for 3 h in a rotary evaporator at atmospheric temperature and pressure. Then, the solution was heated in a water bath at 60 °C, and the pressure conditions were changed to produce a vacuum. The initial pressure was 810 mbar and the final pressure was 100 mbar, for 150 min. After the solution evaporated, the material was taken out to dry in an oven for 24 h at 120 °C. Finally, the material was ground, and the catalyst was ready to be oxidized or reduced.

2.4. Process to Oxidise or Reduce the Synthesized Nanoparticles

The processes for the oxidized and reduced states of the catalyst have been reported before [16]. The reduction process was carried out in a stainless-steel reactor such that hydrogen could be passed through the material. The reduction was carried out for 4 h under a hydrogen flux of 120 cm³/s and a temperature of 500 °C. After this process, the material was placed in a desiccator for 24 h. After the material reached ambient temperature, it was ground and labelled as the reduced form of the catalyst by the sol–gel method, and at the proper metal proportion (Ru or Au) of 1 wt.% or 3 wt.%. For the oxidized state of the metal in the support, the product ready to be oxidized was calcined for 4 h at 500 °C. After that time, the material was placed in a desiccator for 24 h. Table 1 shows the list of the prepared catalysts.

Table 1. List of catalyst prepared by sol–gel TiO₂ support.

Catalyst ID Name	Metal	% of Metal	Oxidation State of Metal
Sol–gel support	-	-	Oxidized
P25 support	-	-	Oxidized
Au 1R	Au	1	Reduced
Au 3R	Au	3	Reduced
Ru 1R	Ru	1	Reduced
Ru 3R	Ru	3	Reduced
Au 1O	Au	1	Oxidized
Au 3O	Au	3	Oxidized
Ru 1O	Ru	1	Oxidized
Ru 3O	Ru	3	Oxidized

2.5. Characterisation Techniques

The synthesized nanomaterials were characterized by X-ray diffraction (XRD) to determine their phases and crystallinity. This was carried out using an Empyrean by Malvern Panalytical, Almelo, equipped with Cu-K α radiation ($\lambda = 0.154$ nm). The surface area was calculated using the standard Brunauer, Emmett, and Teller (BET) method using nitrogen physisorption in a Micromeritics ASAP 2020. With this equipment, the pore size distribution (PSD) was determined using the adsorption branch of isotherms. TiO₂ supports with gold and ruthenium nanoparticles at different percentages were also analysed by XRD. By carrying out the deconvolution of the XRD spectra, it was possible to calculate the particle size using the Debye–Scherrer Equation (1) [17].

$$\tau = \frac{K\lambda}{\beta \cos \theta} \quad (1)$$

where τ is particle size; K is the shape factor, for this work = 0.9; λ is the X-ray wavelength; and β is the line broadening at half the maximum intensity (FWHM), which was determined using Origin Pro software (2018, Northampton, MA, USA). The multiple peak fit function was used with nonlinear curve fitting and θ is the Bragg angle.

The presence of elements in the catalyst, the percentage of each element, and the oxidation state of elements in the catalyst were determined using X-ray photoelectron spectrometry (XPS) Phoipos 150 and Raman spectroscopy (Cora 5500 Anton Paar). The atomic relations are based on the quantification method [18] using Equation (2).

$$\%n_f = (I_{ij}/\sigma_{ij}KE^{0.7}) / \sum (I_{ij}/\sigma_{ij}KE^{0.7}) \quad (2)$$

where I_{ij} is the peak area of the element to be analysed; σ_{ij} is the relative sensitive factor, also known as the Scofield photoemission cross section; and KE is the kinetic energy in eV of the peak.

The UV–vis (UV–visible) spectrophotometer (Shimadzu UV-2600) was used to determine the energy level of the band gap for all catalyst samples. In an investigation of the optical and electrical properties of germanium, a method was proposed for determining the band gap using absorbance plotted versus energy, using the Tauc method [19]. This was later used by Davis and Mott on amorphous semiconductors. The difference between the energy and band gap is the strength of the optical absorption, as shown in Equation (3).

$$(\alpha h\nu)^{\frac{1}{n}} = A(h\nu - E_g) \quad (3)$$

where h is Planck's constant, ν is the photon's frequency, α is the absorption coefficient, E_g is the band gap energy, and A is a proportionality constant. For this experiment, $n = 2$ for indirect allowed transitions. Thus, the basic procedure for the Tauc method is to plot absorbance for the sample in a range of energies from below the band gap transition to above it, $(\alpha h\nu)^{1/n}$ versus $(h\nu)$.

The phase content of anatase and rutile was calculated thanks to the XRD intensity of the characteristic peaks of the phases [20,21], as shown in Equation (4).

$$W_A = \frac{K_A I_A}{(K_A I_A + I_R)} \quad (4)$$

where W_A is the mole fractions of anatase; I_A and I_R are the X-ray integrated intensities of the anatase and the rutile, respectively; and $K_A = 0.886$.

3. Results and Discussion

3.1. Support Characterisation

X-ray diffraction (XRD) was performed to determine the crystallinity of the elements that are present in the catalyst. The first goal is to evaluate the content of the anatase and rutile phases in the supports. In Figure 1, the diffraction spectra for TiO₂ by sol–gel and P25 are shown. The characteristic 2 θ angles for anatase are 25.28, 37.80, 48.05, 53.89, 62.35, 70.12, and 76.35 (JCPDS no. 21-1272), and those for rutile are 27.45, 36.03, 41.23, 44.00, 54.52, 56.95, and 64.01 (JCPDS no. 21-1276) [22].

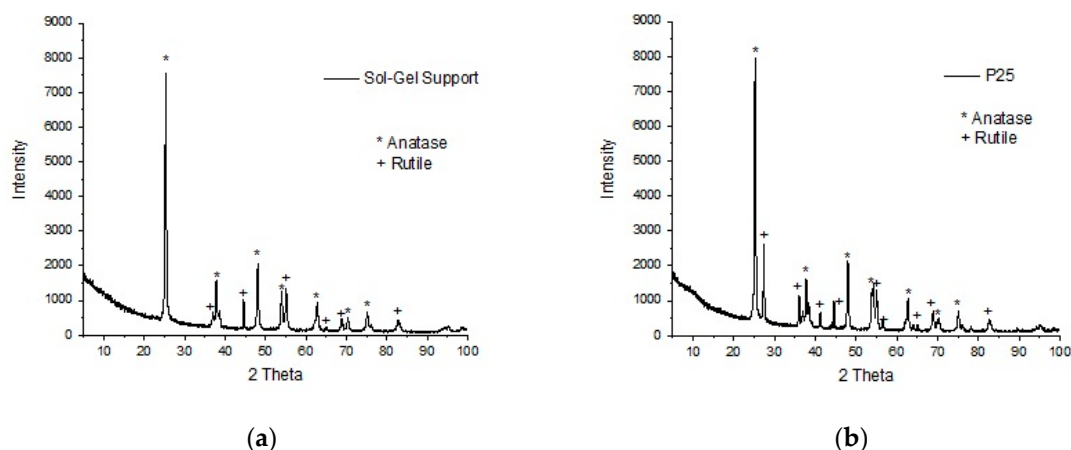


Figure 1. (a) X-ray diffraction (XRD) for TiO₂ support of sol–gel; (b) XRD for TiO₂ P25.

The data show that there is a mix of anatase and rutile in the sol–gel support, where the anatase content is more than 98%. The phase content was calculated using Equation (4), where the anatase phase determination used the plane (101) for 25.28 degrees, and the rutile phase determination used the plane (110) for 27.45 degrees. There are works reporting that anatase is a better photocatalyst than rutile thanks to the longer (2x longer) exciton diffusion in anatase compared with rutile. There are three main reasons why anatase is a better photocatalyst than rutile. Firstly, charge carriers may be trapped and recombined at the interface. Secondly, in the interference, the lattice matching promotes some stress in the support that could affect the surface diffusion. Thirdly, there could be some imperfections, or defects, formed in the surface because of the lattice mismatch, and this leads to a variation in thickness [23].

Another important aspect in the characterisation of the TiO₂ support is the nitrogen physisorption experiments. With these, it was found that the supports had a pore diameter of 264.11 Å (Angstrom) (26.41 nm) and a surface area of 31.25 m²/g. This surface area is low compared with other TiO₂ supports reported by other authors [24], and is in the range of mixed support areas, but with a high concentration of anatase. The ruthenium/anatase content affects the surface area, as it has been reported that, with a support mixture of 80/20% anatase/rutile, the surface area was 70 m²/g; with 100% anatase, the surface area was 250 m²/g; and with 100% rutile, the surface area was 126 m²/g. However, there is no direct correlation between the surface area and photoactivity. For example, in the degradation of lactic acid, the presence of anatase is more important than the surface area [24]. Therefore, to improve the photocatalytic activity, the percentage of anatase in the support has a greater influence than the surface area [23]. The isothermals for the sol–gel support are shown in Figure 2a,d. It can be deduced that the sol–gel support acts as a Type IV for solid mesoporous materials with a Type H1 tie hysteresis according to the International Union of Pure and Applied Chemistry (IUPAC); the pore distribution is very narrow, like the geometry of an open cylinder in the extremes.

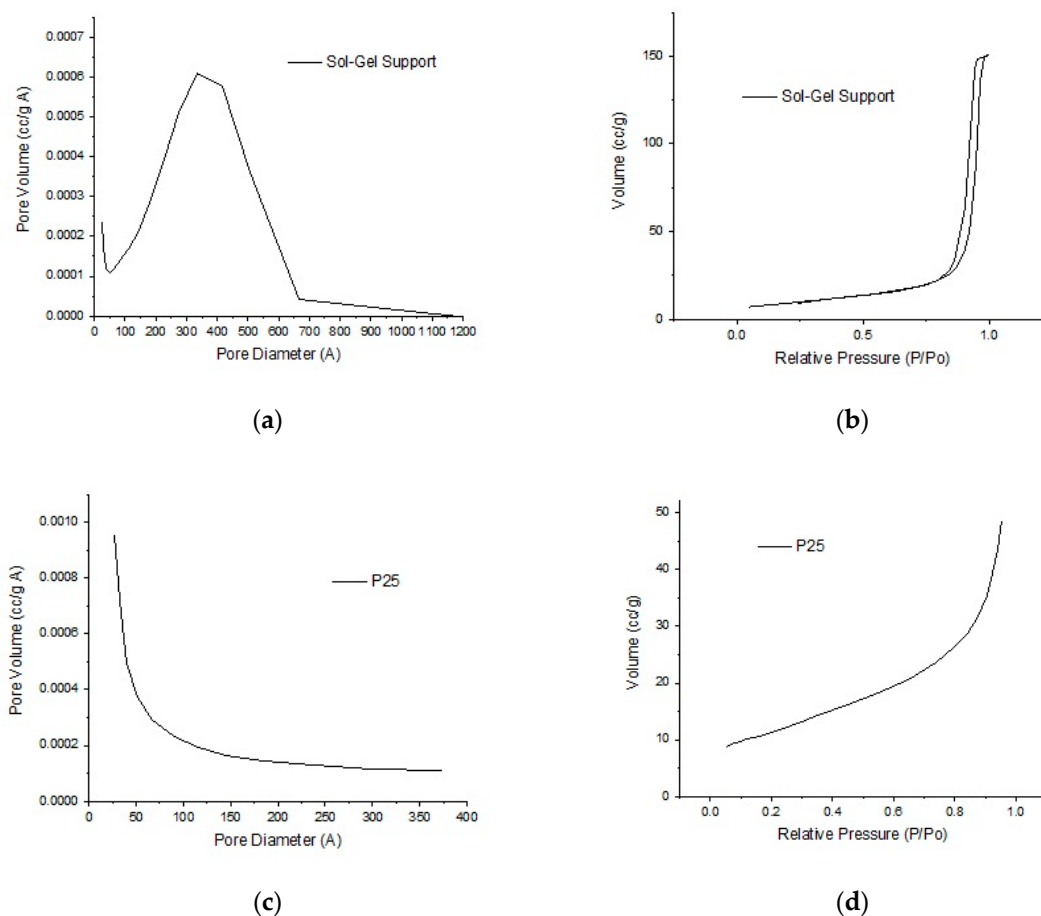


Figure 2. The isothermals for the sol-gel support: (a) N₂-physorption isothermal for pore volume and pore diameter for the sol-gel support, (b) N₂-physorption isothermal for relative pressure and volume for the sol-gel support, (c) N₂-physorption isothermal for pore volume and pore diameter for P25 support, (d) N₂-physorption isothermal for relative pressure and volume for P25 support.

3.2. Catalysts' Characterisation

3.2.1. X-ray Diffraction (XRD)

To determine the elements that are present in the catalyst, X-ray diffraction was carried out. The characteristic 2θ angles for ruthenium are 27.3, 34.9, 40.4, 44.7, and 54.0 degrees [25]. However, in Figure 3a,c, which represent the catalysts with 1 and 3 wt.% ruthenium, respectively, the presence of ruthenium is not clear. This is because the size of the ruthenium nanocrystals is less than 3.0 nm and cannot be detected with X-ray diffraction, which is in accordance with the work of another author [26]. On the other hand, the characteristic 2θ angles for anatase at 25.28, 37.80, 48.05, 53.89, 62.35, 70.12, and 76.35 degrees, and for rutile at 27.45, 36.03, 41.23, 44.00, 54.52, 56.95, and 64.01 degrees, are clearly present [22].

In the case of the catalysts with 1 and 3 wt.% gold (Figure 3b,d), the characteristic peaks of rutile and anatase are also present, and the characteristic peaks of gold at 38.3, 44.6, 64.7, 77.7, and 81.8 degrees are clear [13]. The difference in these catalysts is the intensity of the gold peaks; the higher the amount of gold at 3 wt.%, the higher the intensity of the peaks compared with the smaller amount of gold at 1 wt.%.

With the XRD data and using the Debye-Scherrer equation, it was possible to calculate the particle size of the catalysts, the results of which are shown in Table 2. All the particles have a size less than 100 nm; therefore, it can be called a nano-catalyst [27]. In previous works, it is reported that the XRD of the supported Ru catalysts shows they display a similar behaviour to those of the corresponding TiO₂

support. There are no diffraction peaks of any form of Ru metal or oxides. It has been reported that the presence of Ru with a small particle size may not be detected by XRD and is also viewed when Ru is supported on a TiO₂ support [26,28].

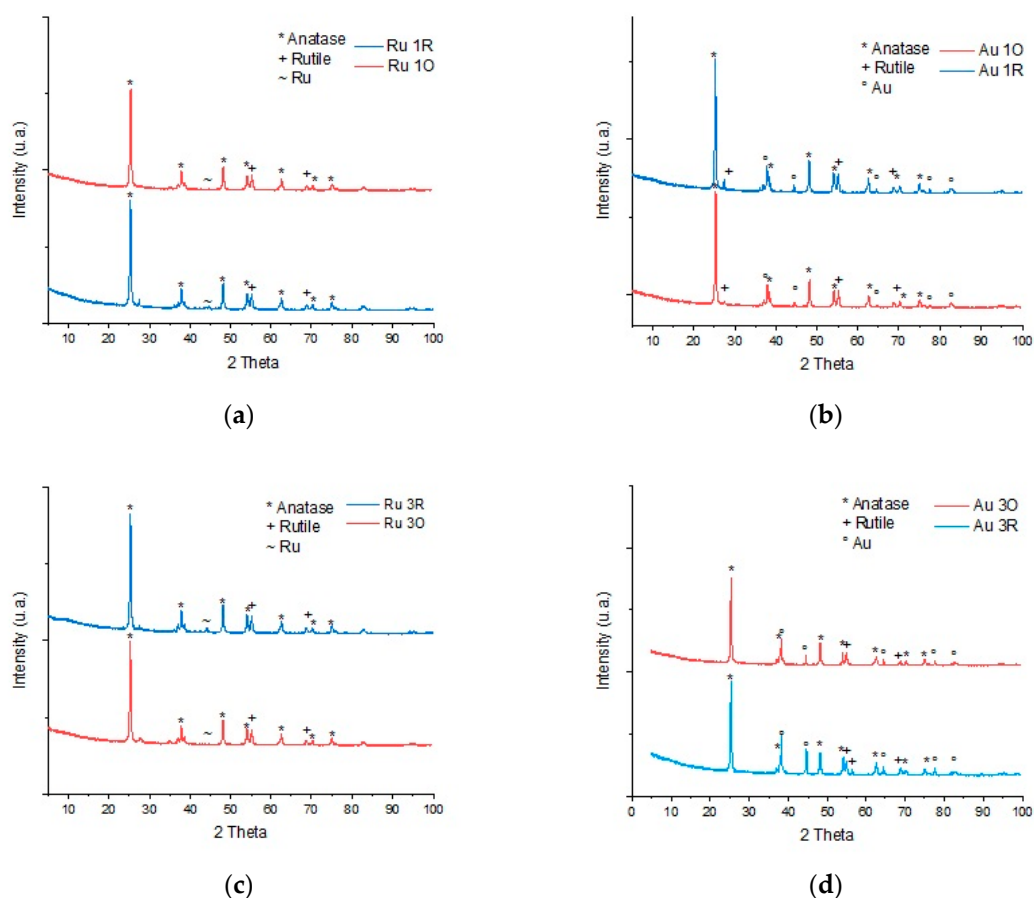


Figure 3. X-ray diffraction (XRD) for catalyst: (a) Ru at 1 wt.%, (b) Au at 1 wt.%, (c) Ru at 3 wt.%, and (d) Au at 3 wt.%.

Table 2. Particle size using the Debye–Scherrer equation with XRD data.

Catalyst ID Name	Anatase (nm)	Au (nm)	Ru (nm)
Sol-gel support	24.08	-	-
Au 1R	24.64	14.92	-
Au 3R	23.50	13.86	-
Ru 1R	20.85	-	<10 *
Ru 3R	23.07	-	<10 *
Au 1O	28.70	12.84	-
Au 3O	27.62	15.62	-
Ru 1O	24.25	-	<10 *
Ru 3O	26.19	-	<10 *

* The presence of Ru with a particle size less than 3.0 nm is beyond the XRD detection limits.

3.2.2. X-ray Photoelectron Spectrometry (XPS)

The XPS spectra of the catalysts of Ru 1–3 wt.% and Au 1–3 wt.% are shown in Figure 4. In each figure, the energy levels are denoted, as well as the respective losses and the Auger electrons. For the determination of the catalyst's components, the cross section was used with a source of aluminium with a special focus on the energy levels that are characteristic for each element [29]. The more characteristic

energy levels for Ru are 3d, 3p, and 3s; for Au, they are 4f and 4d; for Ti, they are 2p, 2s, and 3p; and for O, they are 1s and 2s. This is an important order for each element that will be analysed in the XPS.

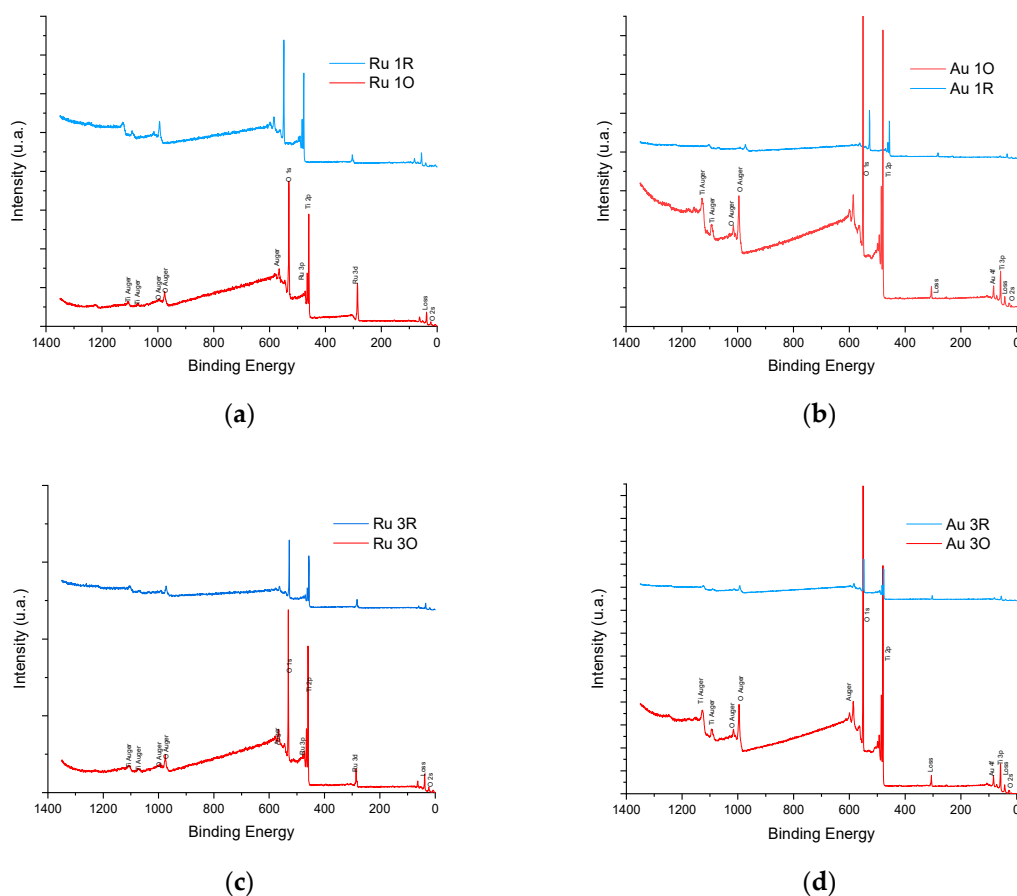


Figure 4. (a) X-ray photoelectron spectrometry (XPS) for catalyst for Ru at 1 wt.%; (b) XPS for catalyst for Au at 1 wt.% (c) XPS for catalyst for Ru at 3 wt.%; (d) XPS for catalyst for Au at 3 wt.%.

Using the information given by the XPS spectra, it was possible to make the deconvolutions using the AAnalyzer software by RDATAA to determine the oxidation state of the metal with the background baseline analysis of the Shirley–Sherwood method [30]. The total area of the peak for oxygen 1s was determined for each one of the catalysts. The information given by the main energy levels of each element can enable the determination of the atomic relation of the element (metal) in the catalyst. Table 3 summarises the percentage of the oxidation state of the metal in the catalyst and the atomic relation to determine the amount of metal in the catalyst. The catalysts were made under a design showing, in the atomic relation, a proper proportion of metal in the catalyst using Equation (2) and XPS data. With the XPS analysis, it can be concluded that there is a difference between the oxidized and reduced state of the metal. The relation of the oxidation state in the catalysts is 70/30. That is, there is not a pure oxidation state of the catalyst or a pure reduced state of the catalyst, but there is a mix of the oxidation states of the metal.

An example of the spectra of an element in its oxidized and reduced state, and the oxygen content, is shown in Figure 5a for Ru 3 wt.% oxidized, and Figure 5b for Ru 3 wt.% reduced. In these figures, it can be seen that there is a chemical shift between the reduced and oxidized state of the metal, and it is clear that the chemical shift in the reduced state is to the right, that is, to lower binding energy levels.

Figure 6 shows the oxygen 1s content of the Ru at 3 wt.%, both oxidized and reduced. By comparing the oxidized and reduced forms (Figure 6a,b), the difference in the level of intensity of the oxygen 1s peak is remarkable; the oxidized state has a stronger intensity than the reduced intensity. In the

oxidized form of the metal, the oxygen peak O 1s has an intensity around 50,000, and in the reduced form of the metal, the oxygen peak O 1s has an intensity around 20,000. When comparing the peak areas of the catalyst with oxygen, and the metal, at a characteristic binding energy, the relation between the oxidized and reduced states can be calculated. Therefore, in this work, there is neither a pure oxidized catalyst nor a pure reduced catalyst; proportions are around 70/30. This behaviour is also present in the energy levels for gold in 4f because the chemical shift is also there and the amount of oxygen between the oxidized and reduced state also has a different proportion of intensity (peak area) in O 1s.

Table 3. X-ray photoelectron spectrometry (XPS) analysis to determine the oxidation state of the metal and the atomic relation in the catalysts.

Catalyst ID Name	Atomic Relation (%)	Oxidation Metal (%)
Au 1R	1.3	<30
Au 3R	3.7	<30
Ru 1R	1.8	<30
Ru 3R	3.2	<30
Au 1O	1.3	>70
Au 3O	3.0	>70
Ru 1O	1.4	>70
Ru 3O	2.8	>70

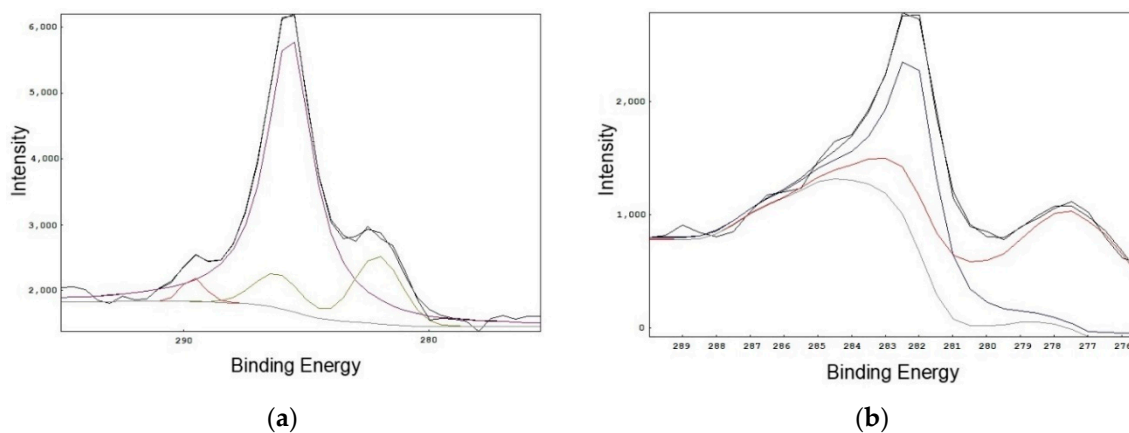


Figure 5. Deconvolutions for determination of the oxidation state of the metal: (a) Ru 3 wt.% oxidized, Ru 3d (3/2, 5/2) and (b) Ru 3 wt.% reduced, Ru 3d (3/2, 5/2).

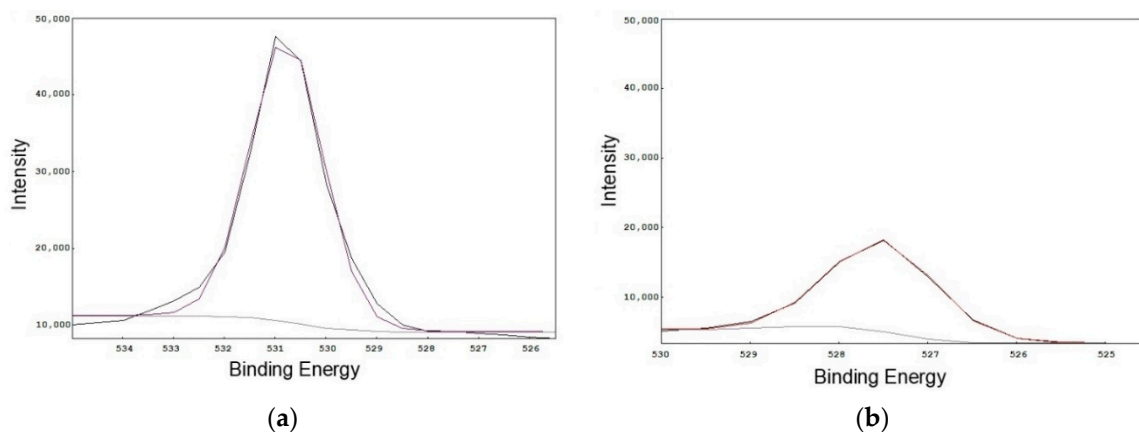


Figure 6. (a) Ru 3 wt.% oxidized O 1s and (b) Ru 3 wt.% reduced O 1s.

3.2.3. Raman Spectroscopy

The presence of anatase and rutile in the catalysts was corroborated with Raman spectra. Anatase has representative peaks or active Raman modes at A 1g (515 cm^{-1}), 2 B 1g ($397, 519\text{ cm}^{-1}$), and 3 E g ($144, 197, 639\text{ cm}^{-1}$) [31]. Rutile modes are at A 1 g (612 cm^{-1}), B 1 g (143 cm^{-1}), B 2 g (826 cm^{-1}), and E g (447 cm^{-1}) [32,33]. Figure 7 shows the Raman spectra of the catalyst of gold supported in TiO_2 in both the oxidized and reduced forms. The support that was prepared has 98% of anatase, as shown in Figure 1. In Raman spectra, there is a behaviour of the catalyst if the rutile proportion in the support is larger than we reported. This behaviour has been reported previously [34]. It appears that the gold improves the rutile signal selectively, perhaps by a surface enrichment effect as used in enhanced Raman spectroscopy. Regardless of the possible reasons, it implies that rutile always occurs in proximity to the gold nanoparticles because no significant rutile formation is observed in Figure 7. That explains the peak's behaviour, but between the oxidized and reduced state of gold, there is a shift in the Raman spectra. The anatase Eg (1) in the reduced state has a Raman shift of 144 versus the anatase Eg (1) in the oxidized state with a Raman shift of 147. Between these two catalysts, a shift of 3 cm^{-1} is observed because of the oxidation process of the catalyst [35].

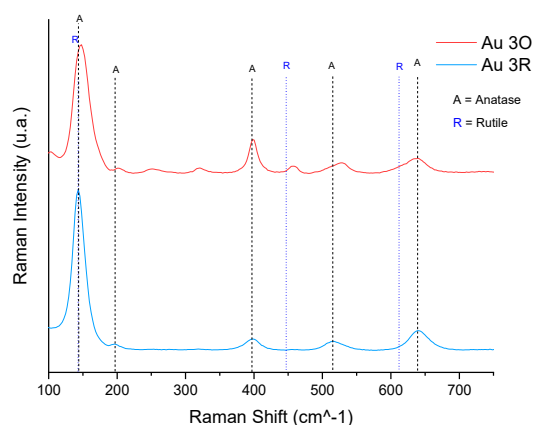


Figure 7. Raman spectra for Au in the oxidized and reduced state of the metal.

In Figure 8, the Raman spectra of the ruthenium catalysts are shown. There is a shift between the oxidized and reduced state of the metal, gold, the shift being 3 cm^{-1} . The presence of ruthenium in the catalyst is better explained with the peak at 528 cm^{-1} . The Raman spectra of RuO_2 are described by three Raman models: Eg, A1g, and B2g at 523 cm^{-1} , 640 cm^{-1} , and 708 cm^{-1} respectively. The A1g and B2g of ruthenium overlaps with the ones of anatase, which is why the observation of these peaks is difficult in Ru/TiO_2 [36]. The Raman shift of 10 cm^{-1} for rutile in Eg after adding ruthenium has been described by the mechanical strains created from the disparities between the rutile phase of RuO_2 and TiO_2 support, as both have rutile [37]. The reduction in H_2 atmosphere of RuO_2 to Ru^0 also shifts the position and width of the anatase. The width of the anatase peaks in reduced ruthenium is narrower than in the oxidized ruthenium state, primarily the 2B1g mode of anatase at 197 cm^{-1} .

3.3. UV/Vis for Band Gap

The absorbance of the catalysts was evaluated using UV/vis equipment and Figure 9 shows the pattern of the absorbance versus the wavelength. The TiO_2 support has two crystallisation forms, anatase and rutile, with the band gap for each one being 3.26 eV and 3.05 eV, respectively [38]. The different crystallographic orientations of the same material may exhibit different activities [23]. In TiO_2 , the phase anatase has a larger band gap energy than rutile. This reduces the light absorbed, but the valence band will increase to higher energy levels. The oxidation power increases and the electron transfer from TiO_2 to the substrate is facilitated [39,40]. Because of that, the catalyst with the

larger band gap will have a better performance in UV light. To obtain the band gap, the graph was plotted for $ah\nu$ versus eV. Figure 10a shows the catalysts plots in the reduced state of the metal and Figure 10b shows the catalysts plots in the oxidized state of the metal.

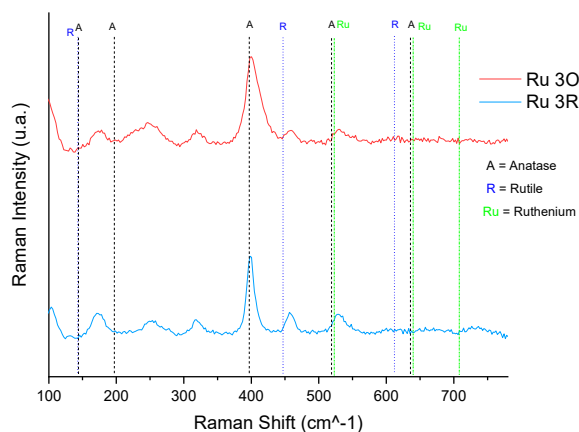


Figure 8. Raman spectra for Ru in the oxidized and reduced state of the metal.

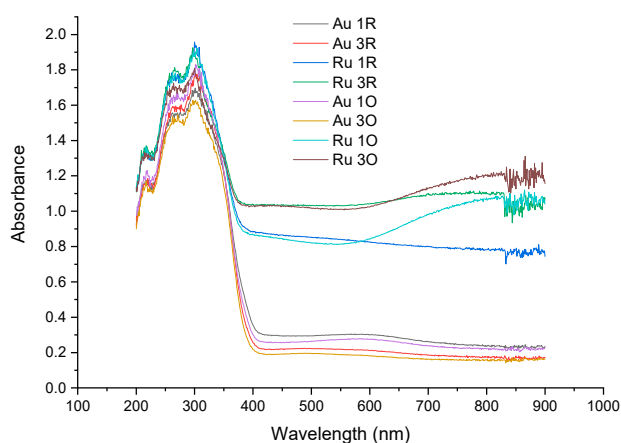


Figure 9. Absorbance versus wavelength in UV/vis spectra of all catalysts.

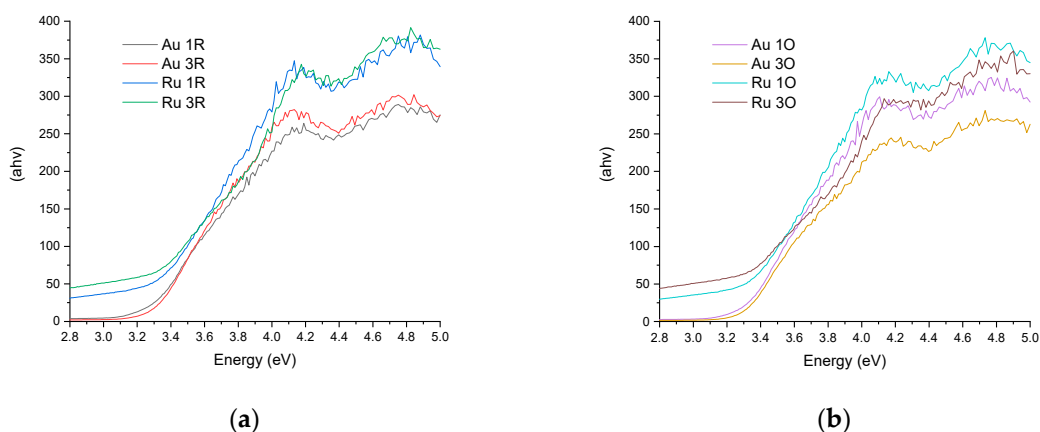


Figure 10. (a) Catalysts plots in the reduced state of the metal and (b) catalysts plots in the oxidized state of the metal.

From Figure 10, the band gap obtained for the catalysts is shown in Table 4 along with the band gap energy and wavelengths that correspond to that band gap. The goal is to narrow the band gap

of the catalyst to improve the optical absorption in the visible wavelength region. The UV region is 100–400 nm. For that, the UV-A region is 315–400 nm, the UV-B region is 280–315 nm, and the UV-C region is 100–280 nm. The visible light region is 400–750 nm [41].

Table 4. Band gap energy and wavelengths.

Catalyst ID Name	Band Gap (eV)	Wavelengths (nm)
Rutile	3.05	406.5
Anatase	3.26	380.3
Sol-Gel Support	3.26	380.3
P25	3.20	387.8
Au 1R	3.25	381.5
Au 3R	3.24	382.7
Ru 1R	3.21	386.2
Ru 3R	3.13	396.1
Au 1O	3.27	379.1
Au 3O	3.25	381.5
Ru 1O	3.21	386.2
Ru 3O	3.11	399.0

From Table 4, there are two catalysts that have a band gap near to the visible light region. These catalysts are ruthenium supported on TiO₂ at 3 wt.% in both the reduced and oxidized metal state, and these catalysts could have some activity in visible light. The outcomes for the band gap indicate that all the catalysts can respond to UV light. For UV light alone, the better rated band gap catalysts are the Au, either 1 wt.% or 3 wt.%, but in the oxidized form of the metal.

4. Conclusions

In the work presented, the sol-gel method with alkoxide was used to obtain an effective support for a TiO₂ catalyst with a high content of anatase. Fabrication of the support was accomplished through the use of gold or ruthenium at various concentrations and oxidation states. Unlike commercial anatase supports, the catalyst support reported here exhibited lower surface area, which is detrimental for catalytic capacity. The support fabricated for these investigations was mesoporous with a narrow pore distribution that resembled open cylinders at the extremes.

XRD analysis of the catalysts showed the presence of metals at the designed proportion. XPS analysis was used to detect particle sizes with 15 nm diameters, and support structures at 25 nm. In XPS analysis, the ruthenium is detectable with the proper designed proportion, which is shown in the atomic relation of the catalyst. In addition, all the designed catalysts showed, in the atomic relation, a proper proportion of metal in the catalyst. With the XPS analysis, it can be concluded that there is a difference between the oxidized and reduced state of the metal. The relation of the oxidation state in the catalysts is 70/30. That is, there is not a pure oxidation state of the catalyst or a pure reduced state of the catalyst, there is a mix of both oxidation states of the metal.

The Raman analysis confirmed the presence of anatase, as well as gold and ruthenium. In addition, the proportions of metals in the catalyst are the designed ones and agree with those calculated in the XPS analysis regarding the metal content and the proportion of the metallic oxidation states. At this point, the catalysts were characterized and found to be in accordance with the design. The goal is to know the photocatalytic activity of each catalyst. The anatase content indicates that photoactivity in the UV region will be take place. With UV/vis analysis, the photoactivity of the catalysts was determined for the UV region and for the UV/visible region. The best catalyst for the UV region is the Au/TiO₂ at 1 wt.% in the oxidized state of the metal. Thanks to the aggregation of the metals, the dosage, and the oxidation state of the metals, the best photocatalytic activity in the visible region is achieved with Ru/TiO₂ at 3 wt.% in the oxidized state of the metal. It can be concluded that, for the UV region, the better catalysts are the gold content ones in the oxidized state of metal; while for the

UV/visible region, the better catalysts are the ruthenium content ones in the oxidized state of metal. The oxidized state of the metal is preferred for both the UV region and the UV/visible region. For the UV region, the gold content catalyst is preferred and, for the UV/visible region, the ruthenium catalysts are preferred. In the future, it is recommended that photocatalytic degradation of the organic components be carried out so that the catalytic performance of the catalysts can be evaluated.

Author Contributions: Methodology, O.R.F.-C. and C.A.G.G.; formal analysis, A.P.-L., O.R.F.-C., and C.A.G.G.; writing—original draft preparation, O.R.F.-C.; writing—review and editing, B.S.-R. and V.H.R.A.; supervision, C.A.G.G. All authors have read and agreed to the published version of the manuscript.

Funding: This research received no external funding.

Acknowledgments: A graduate scholarship for Omar Ricardo Fonseca Cervantes was provided by the National Council for Science and Technology (CONACyT) of México.

Conflicts of Interest: The authors declare no conflict of interest.

References

1. Barakat, M.A. New trends in removing heavy metals from industrial wastewater. *Arab. J. Chem.* **2011**, *4*, 361–377. [[CrossRef](#)]
2. Borges, M.E.; Sierra, M.; Cuevas, E.; García, R.D.; Esparza, P. Photocatalysis with solar energy: Sunlight-responsive photocatalyst based on TiO₂ loaded on a natural material for wastewater treatment. *Sol. Energy* **2016**, *135*, 527–535. [[CrossRef](#)]
3. Malato, S.; Fernández-Ibáñez, P.; Maldonado, M.I.; Blanco, J.; Gernjak, W. Decontamination and disinfection of water by solar photocatalysis: Recent overview and trends. *Catal. Today* **2009**, *147*, 1–59. [[CrossRef](#)]
4. Herrmann, J.M. Heterogeneous photocatalysis: Fundamentals and applications to the removal of various types of aqueous pollutants. *Catal. Today* **1999**, *53*, 115–129. [[CrossRef](#)]
5. Zhang, F.-S.; Itoh, H. Photocatalytic oxidation and removal of arsenite from water using slag-iron oxide-TiO₂ adsorbent. *Chemosphere* **2006**, *65*, 125–131. [[CrossRef](#)]
6. Lin, L.; Wang, K.; Yang, K.; Chen, X.; Fu, X.; Dai, W. The visible-light-assisted thermocatalytic methanation of CO₂ over Ru/TiO(2-x)Nx. *Appl. Catal. B Environ.* **2017**, *204*, 440–455. [[CrossRef](#)]
7. Mirescu, A.; Berndt, H.; Martin, A.; Prüße, U. Long-term stability of a 0.45% Au/TiO₂ catalyst in the selective oxidation of glucose at optimised reaction conditions. *Appl. Catal. A Gen.* **2007**, *317*, 204–209. [[CrossRef](#)]
8. Zhang, J.; Huang, Q.-A.; Wang, J.; Wang, J.; Zhang, J.; Zhao, Y. Supported dual-atom catalysts: Preparation, characterization, and potential applications. *Chin. J. Catal.* **2020**, *41*, 783–798. [[CrossRef](#)]
9. Gopinath, K.; Madhav, N.; Krishnan, A.; Malolan, R.; Rangarajan, G. Present applications of titanium dioxide for the photocatalytic removal of pollutants from water: A review. *J. Environ. Manag.* **2020**, *270*, 110906. [[CrossRef](#)]
10. Ninsonti, H.; Sriwichai, S.; Wetchakun, N.; Kangwansupamonkon, W.; Phanichphant, S. Au-loaded TiO₂ and Ag-loaded TiO₂ synthesized by modified sol-gel/impregnation method as photocatalysts. *Jpn. J. Appl. Phys.* **2016**, *55*, 02BC05. [[CrossRef](#)]
11. Sasirekha, N.; Basha, S.J.S.; Shanthi, K. Photocatalytic performance of Ru doped anatase mounted on silica for reduction of carbon dioxide. *Appl. Catal. B Environ.* **2006**, *62*, 169–180. [[CrossRef](#)]
12. Piskun, A.S.; Ftouni, J.; Tang, Z.; Weckhuysen, B.M.; Bruijninx, P.C.A.; Heeres, H.J. Hydrogenation of levulinic acid to γ -valerolactone over anatase-supported Ru catalysts: Effect of catalyst synthesis protocols on activity. *Appl. Catal. A Gen.* **2018**, *549*, 197–206. [[CrossRef](#)]
13. Peng, X.; Wan, G.; Wu, L.; Zeng, M.; Lin, S.; Wang, G. Peroxidase-like activity of Au@TiO₂ yolk-shell nanostructure and its application for colorimetric detection of H₂O₂ and glucose. *Sens. Actuators B Chem.* **2018**, *257*, 166–177. [[CrossRef](#)]
14. Stephen, A.J.; Rees, N.V.; Mikheenko, I.; Macaskie, L.E. Platinum and Palladium Bio-Synthesized Nanoparticles as Sustainable Fuel Cell Catalysts. *Front. Energy Res.* **2019**, *7*. [[CrossRef](#)]
15. Rodríguez-González, V.; Zanella, R.; del Angel, G.; Gómez, R. MTBE visible-light photocatalytic decomposition over Au/TiO₂ and Au/TiO₂-Al₂O₃ sol-gel prepared catalysts. *J. Mol. Catal. A Chem.* **2008**, *281*, 93–98. [[CrossRef](#)]

16. Ramírez-Salgado, J.; Djurado, E.; Fabry, P. Synthesis of sodium titanate composites by sol-gel method for use in gas potentiometric sensors. *J. Eur. Ceram. Soc.* **2004**, *24*, 2477–2483. [[CrossRef](#)]
17. Bokuniaeva, A.O.; Vorokh, A.S. Estimation of particle size using the Debye equation and the Scherrer formula for polyphasic TiO₂ powder. *J. Phys. Conf. Ser.* **2019**, *1410*, 012057. [[CrossRef](#)]
18. Vickerman, J.; Gilmore, I. *Surface Analysis—The Principal Techniques*, 2nd ed.; John Wiley & Son: Hoboken, NJ, USA, 2009.
19. Coulter, J.; Birnie, D. Assessing Tauc Plot Slope Quantification: ZnO Thin Films as a Model System. *Phys. Status Solidi (b)* **2018**, *255*, 1–7. [[CrossRef](#)]
20. Zhang, H.; Banfield, J.F. Understanding Polymorphic Phase Transformation Behavior during Growth of Nanocrystalline Aggregates: Insights from TiO₂. *J. Phys. Chem. B* **2000**, *104*, 3481–3487. [[CrossRef](#)]
21. He, Z.; Cai, Q.; Fang, H.; Situ, G.; Qiu, J.; Song, S.; Chen, J. Photocatalytic activity of TiO₂ containing anatase nanoparticles and rutile nanoflower structure consisting of nanorods. *J. Environ. Sci.* **2013**, *25*, 2460–2468. [[CrossRef](#)]
22. Ai, C.; Xie, P.; Zhang, X.; Zheng, X.; Li, J.; Kafizas, A.; Lin, S. Explaining the Enhanced Photoelectrochemical Behavior of Highly Ordered TiO₂ Nanotube Arrays: Anatase/Rutile Phase Junction. *ACS Sustain. Chem. Eng.* **2019**, *7*, 5274–5282. [[CrossRef](#)]
23. Luttrell, T.; Halpegamage, S.; Tao, J.; Kramer, A.; Sutter, E.; Batzill, M. Why is anatase a better photocatalyst than rutile?—Model studies on epitaxial TiO₂ films. *Sci. Rep.* **2014**, *4*, 1–8. [[CrossRef](#)] [[PubMed](#)]
24. Holm, A.; Hamandi, M.; Simonet, F.; Jouguet, B.; Dappozze, F.; Guillard, C. Impact of rutile and anatase phase on the photocatalytic decomposition of lactic acid. *Appl. Catal. B Environ.* **2019**, *253*, 96–104. [[CrossRef](#)]
25. Kumar, P.; Kumar, A.; Dev, S.; Naresh; Dhar, R. Effect of thermally co-evaporated Ru-TiO₂ nano-composite thin film against *S. aureus* bacterial biofilm formation. *AIP Conf. Proc.* **2020**, *2220*, 020126. [[CrossRef](#)]
26. Abe, T.; Tanizawa, M.; Watanabe, K.; Taguchi, A. CO₂ methanation property of Ru nanoparticle-loaded TiO₂ prepared by a polygonal barrel-sputtering method. *Energy Environ. Sci.* **2009**, *2*, 315. [[CrossRef](#)]
27. Vert, M.; Doi, Y.; Hellwich, K.-H.; Hess, M.; Hodge, P.; Kubisa, P.; Rinaudo, M.; Schué, F. Terminology for biorelated polymers and applications (IUPAC Recommendations 2012). *Pure Appl. Chem.* **2012**, *84*, 377–410. [[CrossRef](#)]
28. Wang, G.-Y.; Gao, Y.-X.; Wang, W.-D.; Huang, W.-X. Selective CO Methanation over Ru Catalysts Supported on Nanostructured TiO₂ with Different Crystalline Phases and Morphology. *Chin. J. Chem. Phys.* **2012**, *25*, 475–480. [[CrossRef](#)]
29. Yeh, J.J.; Lindau, I. Atomic subshell photoionization cross section and asymmetry parameters. *Atomic Data Nucl. Data Tables* **1985**, *32*, 1–555. [[CrossRef](#)]
30. Végh, J. The Shirley background revised. *J. Electron. Spectrosc. Relat. Phenom.* **2006**, *151*, 159–164. [[CrossRef](#)]
31. Cho, H.-W.; Liao, K.-L.; Yang, J.-S.; Wu, J.-J. Revelation of rutile phase by Raman scattering for enhanced photoelectrochemical performance of hydrothermally-grown anatase TiO₂ film. *Appl. Surf. Sci.* **2018**, *440*, 125–132. [[CrossRef](#)]
32. Gonzalez, R.J.; Zallen, R. Infrared reflectivity and lattice fundamentals in anatase TiO₂. *Phys. Rev. B* **1997**, *55*, 7014–7017. [[CrossRef](#)]
33. Hong, M.; Dai, L.; Li, H.; Hu, H.; Liu, K.; Yang, L.; Pu, C. Structural Phase Transition and Metallization of Nanocrystalline Rutile Investigated by High-Pressure Raman Spectroscopy and Electrical Conductivity. *Minerals* **2019**, *9*, 441. [[CrossRef](#)]
34. Pougín, A.; Lüken, A.; Klinkhammer, C.; Hiltrop, D.; Kauer, M.; Tölle, K.; Havenith-Newen, M.; Morgenstern, K.; Grünert, W.; Muhler, M.; et al. Probing Oxide Reduction and Phase Transformations at the Au-TiO₂ Interface by Vibrational Spectroscopy. *Top. Catal.* **2017**, *60*, 1744–1753. [[CrossRef](#)]
35. Song, L.; Lu, Z.; Zhang, Y.; Su, Q.; Li, L. Hydrogen-Etched TiO₂-x as Efficient Support of Gold Catalysts for Water-Gas Shift Reaction. *Catalysts* **2018**, *8*, 26. [[CrossRef](#)]
36. Vera-Romero, I.; Estrada-Jaramillo, M.; Martínez-Reyes, J.; Ortiz-Soriano, A. Potencial de generación de biogás y energía eléctrica. Parte II: Residuos sólidos urbanos. *Ing. Investig. Tecnol.* **2015**, *16*, 471–478. [[CrossRef](#)]
37. Barkhuizen, D.; Mabaso, I.; Viljoen, E.; Welker, C.; Claeys, M.; van Steen, E.; Fletcher, J. Experimental approaches to the preparation of supported metal nanoparticles. *Pure Appl. Chem.* **2006**, *78*, 1759–1769. [[CrossRef](#)]
38. Carp, O. Photoinduced reactivity of titanium dioxide. *Prog. Solid State Chem.* **2004**, *32*, 33–177. [[CrossRef](#)]

39. Batzill, M. Fundamental aspects of surface engineering of transition metal oxide photocatalysts. *Energy Environ. Sci.* **2011**, *4*, 3275. [[CrossRef](#)]
40. Pan, J.; Liu, G.; Lu, G.Q.M.; Cheng, H.-M. On the True Photoreactivity Order of {001}, {010}, and {101} Facets of Anatase TiO₂ Crystals. *Angew. Chem. Int. Ed.* **2011**, *50*, 2133–2137. [[CrossRef](#)]
41. ISO. 21348 Space environment (natural and artificial)—Process for determining solar irradiances. In *The International Organization for Standardization*; ISO: Geneva, Switzerland, 2007.



© 2020 by the authors. Licensee MDPI, Basel, Switzerland. This article is an open access article distributed under the terms and conditions of the Creative Commons Attribution (CC BY) license (<http://creativecommons.org/licenses/by/4.0/>).